



Characterization and catalytic performance of B-doped, B–N co-doped and B–N–F tri-doped TiO₂ towards simultaneous Cr(VI) reduction and benzoic acid oxidation



A.E. Giannakas^a, M. Antonopoulou^a, C. Daikopoulos^b, Y. Deligiannakis^{b,**},
I. Konstantinou^{a,*}

^a Department of Natural Resources and Environmental Management, University of Patras, G. Seferi 2, Agrinio 30100, Greece

^b Department of Physics, University of Ioannina, Panepistimioupoli Douroutis, Ioannina 45110, Greece

ARTICLE INFO

Article history:

Received 30 June 2015

Received in revised form 3 November 2015

Accepted 7 November 2015

Available online 12 November 2015

Keywords:

Photocatalysis

TiO₂

B, N, F doping

EPR

Cr(VI)

ABSTRACT

B-doped, B–N co-doped and B–N–F tri-doped TiO₂ catalysts were prepared via a sol–gel method using H₃BO₃, NH₄Cl and NH₄F as B, N and N–F dopant precursors, respectively. N-doped, N–F co-doped and a pure TiO₂ (undoped) samples were also prepared by the same method as blank samples, for comparison. The catalysts were evaluated for the simultaneous photocatalytic reduction of Cr(VI) and oxidation of benzoic acid (BA). XRD analysis shows the formation of pure TiO₂ anatase phase in all cases, with crystallite size varying from 10.1 nm to 14.6 nm for all doped samples. UV–vis DRS spectra show narrowing of the band gap (E_g) for all doped samples, compared to the undoped TiO₂. Concomitant presence of N and F ions i.e. in N–F co-doped and B–N–F tri-doped TiO₂ catalysts, causes the most pronounced decrease of E_g while B–N co-doped and B–N–F tri-doped TiO₂ have lower E_g values than mono B-doped but higher than N-doped and N–F doped TiO₂. B and N doping also causes an increase of specific surface area and a decrease in mean pore diameter. Electron Paramagnetic Resonance (EPR) spectroscopy was employed for a detailed investigation of the structure and photoexcited species formed in these catalysts. The EPR data show that N-doping forms N_b[•] photoexcited species which react as holes, Ti⁴⁺–O^{•−} oxygen vacancies (OVs) and Ti³⁺ lattice and surface defects. B-doping enhances the formation of Ti⁴⁺–O^{•−} oxygen vacancies and the quantities of [•]O₂H and [•]OH radicals. In B-doped and B–N co-doped samples, boron causes the most prominent induction of Ti³⁺ lattice centers. Boron in interstitial sites, with oxygen atoms [BO₃] behaves as a three-electron donor leading to the formation of B³⁺ and reduction of Ti⁴⁺ to Ti³⁺. Under UV–vis irradiation, Cr(VI) reduction followed the trend: TB1 > TBN1 > TBNF1 > TNF1 > TN1 > undoped TiO₂; while benzoic acid (BA) oxidation trend was: TB1 > TBNF1 > TBN1 > TNF1 > TN1 > undoped TiO₂. Cr(VI) reduction and BA oxidation rates are in agreement with EPR-detected Ti⁴⁺–O^{•−} oxygen vacancies and [•]O₂H, [•]OH photoexcited radicals, respectively.

© 2015 Elsevier B.V. All rights reserved.

1. Introduction

Semiconductor photocatalysis is a very important technology for many environmental applications because it can utilize solar energy to decompose harmful organic and inorganic pollutants present in air and aqueous systems. Titanium dioxide (TiO₂) is the most promising photocatalyst because of its high efficiency, low cost, chemical inertness, and high photo-stability [1,2]. The major drawbacks of TiO₂-based photocatalysts arise [i] from the

rapid electron–hole pair recombination that suppresses the quantum efficiency, and [ii] the wide band-gap (3.0 eV for rutile and 3.2 eV for anatase), which restricts light absorption to only ultraviolet region (wavelength < 390 nm), thus limiting the practical field applications of TiO₂-based photocatalysts for solar light harvesting [3]. It is, therefore, a priority need to develop visible-light active TiO₂ photocatalysts e.g., via structural modification or doping of TiO₂.

Since the report by Asahi et al. [4] revealing that nitrogen-doping can significantly improve the visible-light photocatalytic activity of TiO₂, there it has been a fruitful research strategy to narrow the band gap of TiO₂ by doping it with non-metal ions, leading to broader light response range towards visible wavelengths. In this context, significant progress has been made in TiO₂ doped with non-metal ions [5], such as B [6–8], C, N, S, F [9–12]. More recently,

* Corresponding author.

** Corresponding author.

E-mail addresses: ideligia@cc.uoi.gr (Y. Deligiannakis), iokonst@upatras.gr, iokonst@cc.uoi.gr (I. Konstantinou).

a more efficient approach has emerged, that is TiO₂ materials co-doped with two kinds of nonmetal atoms such as N–F, N–I, N–S and N–C [13–16]. In these TiO₂–N–X (X = F, I, S, C) materials one of the doping atoms is N, which is expected to profit from a synergistic effect of the co-dopant X, permitting a fine-tuning of the electronic structure of TiO₂–N–X enhancing in this way the photocatalytic activity.

In TiO₂–N, substitutional doping with N has been proven [17] to be a good candidate for band-gap narrowing of TiO₂ i.e., since N2p states can mix with O 2p states efficiently. In addition, in TiO₂–N catalysts the N atom is bound to a lattice–oxygen atom thus giving rise to a paramagnetic species with the unpaired electron in one of the π^* orbitals of the N–O fragment called N_b species (b: bulk) [17] which can be determined using Electron Paramagnetic Resonance (EPR) spectroscopy [13,17,18].

Apart from N doped TiO₂ catalysts, B–N co-doping has shown promising photo-response [19–24] however – so far – the catalytic performance of B–N–TiO₂ has not been fully exploited. Recently, In et al. [19] reported that B–N co-doped TiO₂ exhibits enhanced photocatalytic activity under UV and visible light irradiation, which is probably attributed to the synergistic effect between boron and nitrogen, resulting the narrowing of the band gap. Wu et al. [20] using an one-step combustion reaction prepared N–B co-doped TiO₂ catalysts that exhibited improved visible light response, while Zhang et al. [21] focused on the modification of the crystalline structure of TiO₂ and improvement of the specific surface area. Gopal et al. [23] and Czoska et al. [24] studied N–B co-doped TiO₂ particles with EPR spectroscopy and detected two kinds of paramagnetic species. The first center is the well characterized [N_iO][•] species (i = interstitial) which are also present in N-doped TiO₂ [23,24], while the second one involves both N and B [23,24]. This latter center (labeled [NOB][•]) exhibits well resolved EPR spectra, obtained using either ¹⁴N or ¹⁵N, which show a high spin density in a N 2p orbital [23]. These [NOB][•] species can contribute to the visible light activity [23]. However, both reports [23,24] concluded that the synergistic effect of co-doping on photocatalytic efficiency is another subject that needs to be subjected to detailed catalytic evaluation.

On the other hand, few reports are focused in tri-doped TiO₂ catalysts [25–27]. To the best of our knowledge – so far – only Li et al. [27] have reported the preparation of B–N–F tri-doped TiO₂ photocatalysts via a microwave assisted route and they observed a synergistic effect of N, B and F i.e., and improved photo-generated electron/hole separation efficiency.

Herein, we present the catalytic and spectroscopic study of three photocatalysts B-doped, B–N co-doped TiO₂ and B–N–F tri-doped TiO₂ catalysts, prepared via a sol gel impregnation route. Specific aims of the present work are: [i] to evaluate their photocatalytic performance in simultaneous Cr(VI) reduction and benzoic acid oxidation for the first time, [ii] to perform a detailed in situ trapping-characterization of the various photoinduced active centers, as well as the nitrogen and nitrogen–boron paramagnetic species formed in the N doped, B–N co-doped and B–N–F tri-doped TiO₂ solids by EPR spectroscopy. [iii] to investigate the effect of boron insertion in pure anatase, N doped anatase and N–F co-doped anatase crystals by EPR spectroscopy and providing novel data in photo/redox mechanism of B-doped, B–N co-doped and B–N–F tri-doped TiO₂ catalysts.

2. Experimental

2.1. Preparation of B–TiO₂, B–N–TiO₂ and B–N–F–TiO₂ catalysts

The preparation of B–TiO₂, B–N–TiO₂, and B–N–F–TiO₂ catalysts was based on a sol gel impregnation method, as detailed previously [13,14]. More specifically, 3.4 mL titanium (IV) n-butoxide was

added dropwise to 50 mL aqueous solution containing appropriate amounts of H₃BO₃, H₃BO₃–NH₄Cl, and H₃BO₃–NH₄F to achieve atomic ratios of B/Ti, B–N/Ti, N/Ti, N–F/Ti and B–N–F/Ti equal to 1/1. The choice of 1/1 atomic ratio was based on our previous detailed work [13], where it was shown that N/Ti = 1 and N–F/Ti = 1 was the optimum for the preparation of N-doped and N–F co-doped TiO₂ catalysts. The B/Ti atomic ratio was equal to 1/1 in order to avoid the formation of B₂O₃ impurities according to previous reports [6a,c]. The obtained yellowish milky suspensions were aged for 24 h at room temperature (25 °C) and subsequently dried at 110 °C for at least 48 h. The obtained xerogels were calcined at 500 °C in air for 1 h with ramp rate 5 °C/min. Next, the calcined powders were dispersed in water and the suspensions were sonicated in a water sonication bath for 2 h, then washed with distilled water to remove impurities. Finally, the materials were dried again at 110 °C for 24 h and ground in agate mortar. The so-prepared B-doped, N-doped, B–N co-doped, N–F co-doped and B–N–F tri-doped catalysts herein are code-named as TB1, TBN1, TBNF1. For comparison, N-doped, N–F co-doped and undoped TiO₂ was also prepared by the same protocol and labeled as TN1, TNF1 and ‘undoped-TiO₂’. Full details of the preparation protocol used for each sample, are listed in Table 1.

2.2. XRD analysis

X-ray diffraction patterns were recorded in a Brüker Advance D8 system employing CuK α radiation (λ = 1.5418 Å) in the range 10° < 2 θ < 80° with a resolution of 0.02°/2 θ . Identification of the crystal phases was done using the Joint Committee on Powder Diffraction Standards (JCPDS) data library, and then Rietveld refinement was applied to obtain the crystallite parameters. The results are shown in Fig. 1 and Table 2.

2.3. UV–vis – DRS measurements

The ultraviolet–visible diffusion reflectance spectra (UV–vis DRS) of all samples were measured with the PerkinElmer (Lambda 35) spectrophotometer equipped with an integrating sphere assembly, using BaSO₄ as the reflectance standard at room temperature in the wavelength range of 220–800 nm. The UV–vis diffuse reflectance spectra of all samples are shown in Fig. 2a. In Fig. 2b, the Kubelka Munk plots are included for all prepared samples. The E_g values calculated from Fig. 2b for all catalysts are listed in Table 2 for comparison.

2.4. Surface area and porosity

The specific surface area S_p (m² g^{−1}), as well as the specific pore volume V_p (cm³ g^{−1}), was determined by N₂ adsorption–desorption porosimetry at 77 K via the Brunauer–Emmett–Teller (BET method). The instrument employed was a Sorptomatic 1990, Thermo Finnigan porosimeter. Specific surface area values as well as specific pore volume V_p values for all TiO₂ catalysts are included in Table 2.

2.5. EPR experiments

Electron Paramagnetic Resonance (EPR) spectra were recorded at 77 K with a Brüker ER200D spectrometer, equipped with an Agilent 5310A frequency counter operating at the X band. Adequate signal to noise was obtained after 15 scans. The spectrometer was running under a home-made software based on Lab View [28]. A Xe lamp (450 W, Oriel model 66929) equipped with a water IR cut-off filter was used as the irradiation source. Photogenerated holes and electrons were studied by EPR by illuminating the samples at 77 K

Table 1

The compositions of sols employed for the preparation of B-doped, N doped, B–N co-doped, N–F co-doped and B–N–F tri-doped TiO₂ photocatalysts.

Code name	H ₃ BO ₃ (g–mol)	NH ₄ Cl (g–mol)	NH ₄ F (g–mol)	TBOT (ml–mol)	total sol volume (ml)
TB1	0.6–0.01	–		3.4–0.01	50
TN1		0.53–0.01		3.4–0.01	50
TBN1	0.6–0.01	0.53–0.01		3.4–0.01	50
TNF1			0.37–0.01	3.4–0.01	50
TBNF1	0.6–0.01		0.37–0.01	3.4–0.01	50
Undoped–TiO ₂		–	–	3.4–0.01	50

Table 2

Results of XRD with Rietveld analysis, BET analysis and E_g values of all prepared B-doped, N doped, B–N co-doped, N–F co-doped and B–N–F tri-doped TiO₂ photocatalysts.

XRD rietveld analysis and BET results									
code name	crystal phase	space group	a	c	Crystal size d(nm)	S _p m ² g ^{−1}	V _p cm ³	D _{mean} Å	E _g eV
TB1	Anatase TiO ₂	Tetragonal I41	3.784	9.490	10.9	141.6	0.33	60.0	3.08
TN1	Anatase TiO ₂	Tetragonal I41	3.797	9.538	10.1	115.8	0.45	67.2	3.01
TBN1	Anatase TiO ₂	Tetragonal I41	3.781	9.503	12.2	156.7	0.46	50.0	3.06
TNF1	Anatase TiO ₂	Tetragonal I41	3.788	9.502	14.6	65.3	0.34	191.8	2.91
TBNF1	Anatase TiO ₂	Tetragonal I41	3.787	9.506	13.3	121.2	0.32	95.9	2.94
undoped TiO ₂	Anatase TiO ₂	Tetragonal I41	3.782	9.522	21.0	108.0	0.29	78.2	3.18
TiO ₂ databank phase	Anatase TiO ₂	Tetragonal I41	3.784	9.515	–	–	–	–	–

Table 3

g- and ¹⁴N (I = 1) hyperfine-tensors of observed paramagnetic species in B-doped, B–N co-doped and B–N–F tri-doped TiO₂ With bold font are emphasized the g components detected experimentally.

Paramagnetic species	<i>g</i> ₁	<i>g</i> ₂	<i>g</i> ₃	A ₁ /Gauss	A ₂ /Gauss	A ₃ /Gauss	<i>g</i> ₁	<i>g</i> ₂	<i>g</i> ₃	Ref.
NO	2.001	1.998	1.927	<1	32.2	9.6	–	–	–	[17,18,35]
N _b [•]	2.005	2.004	2.003	2.3	4.4	32.3	–	–	–	[17,18,35]
Ti ³⁺ lattice	–	–	–	–	–	–	1.989	1.964	1.94	[18]
Ti ³⁺ surface	–	–	–	–	–	–	1.972	1.954	1.93	[14,33]
	<i>g</i> _{zz}	<i>g</i> _{yy}	<i>g</i> _{xx}							[33]
O ₂ ^{•−} [I]	2.021	2.009	2.003							[33]
O ₂ ^{•−} [II]	2.0184	2.0096	2.0033							[33]
Ti ⁴⁺ –O ^{•−} –Ti ⁴⁺ –OH ^{•−}	2.024	2.014	2.007							[33]
Ti ⁴⁺ –O ^{2•−} –Ti ⁴⁺ –O ^{•−}	2.028	2.016	2.002							[34]
Ti ⁴⁺ –O ₂ H	2.034	2.009	2.002							
Ti ⁴⁺ –O ^{•−}							<i>g</i> 2.0046		<i>g</i>_⊥ 2.0121	[33]

in situ in the EPR cavity. To measure the maximum photogenerated electrons in the TiO₂ samples, EPR illumination experiments were performed with use of isopropanol, as hole-scavenger [29]. The results of the EPR experiments are represented in Figs. 3–6, and Table 3.

2.6. Photocatalytic experiments and analytical methods.

Photocatalytic experiments under UV–vis irradiation were carried out in a solar simulator Atlas Suntest XLS + from Heraeus (Germany) equipped with a xenon lamp (2.2 kW). The light source was jacked with special glass filters restricting the transmission of wavelengths below 290 nm. The temperature of the sample was maintained at 25 °C using a tap water cooling circuit, preventing any heating of the suspension. An average irradiation intensity of 500 Wm^{−2} was maintained throughout the experiments and was measured by internal radiometer supplied by the manufacturer. Irradiation experiments were performed using a 250 mL Pyrex glass UV-reactor containing 250 mL of binary (Cr(VI) and benzoic acid) aqueous solutions at different pH values. The pH of solutions was adjusted by H₂SO₄ at pH = 2. Visible light (>400 nm) irradiation was performed by a 20 W led flood lamp emitting 1600 lumens. The lamp was positioned 5 cm away from the photoreactor which was a glass cylindrical reactor containing 50 mL of the binary solutions and the appropriate amount of catalysts to achieve the desirable catalyst concentration (500 mg L^{−1}). Relative errors lower than 4.5% between repeated experiments were obtained in all cases.

The solutions were mixed with the appropriate amount of catalyst and were magnetically stirred before and during the illumination. The suspensions were kept in the dark for 30 min, prior to illumination in order to reach adsorption equilibrium onto semiconductor surface. As the reaction progressed, at specific time intervals samples were withdrawn from the reactor for further analysis.

Benzoic acid concentrations were determined by a Dionex P680HPLC chromatography equipped with a Dionex PDA-100 Photodiode Array Detector using a Discovery C18, (250 mm length × 4.6 mm ID; 5 μm particle size) analytical column from Supelco (Bellefonte, PA, USA). The HPLC mobile phase was a mixture of LC-grade water H₂O (70%) pH 3 (adjusted with formic acid) and acetonitrile 30%) with a flow rate of 1 mL/min. Column temperature was set at 40 °C. The detection of benzoic acid was realized at 228 nm. The concentration of Cr (VI) was determined by the diphenylcarbazide colorimetric method [30] at a wavelength of 540 nm using a UV–vis spectrophotometer (Hitachi, U-2000).

3. Results

3.1 XRD analysis

Representative X-ray diffractograms for TB1, TN1, TBN1, TNF1 and TBNF1 solids are shown in Fig. 1. The reflections of TiO₂ anatase phase with tetragonal I41 space group, according to the JCPDS 21-1272 databank, are included in the bottom of Fig. 1 (bar-diagram). All the XRD patterns recorded for all our doped, co-doped or tri-doped TiO₂ materials correspond to pure anatase-TiO₂ (JCPDS

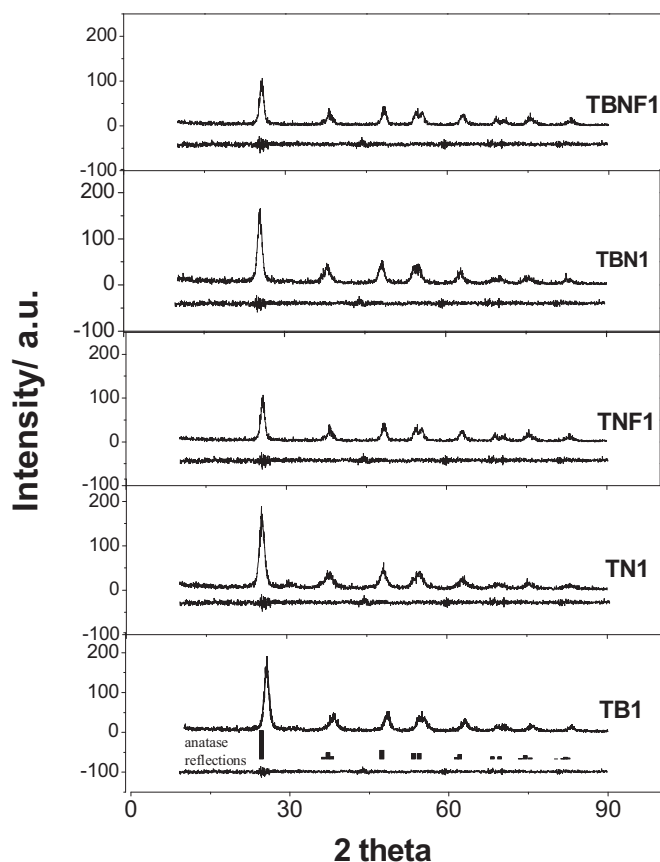


Fig. 1. Representative XRD patterns for all prepared B, N doped, B–N, N–F co-doped and B–N–F tri-doped TiO_2 catalysts. The line plot above TB1 sample represents difference plot between experimental and theoretical calculated (rietveld analysis). Column type plot represents the reflections of TiO_2 anatase phase according to databank used.

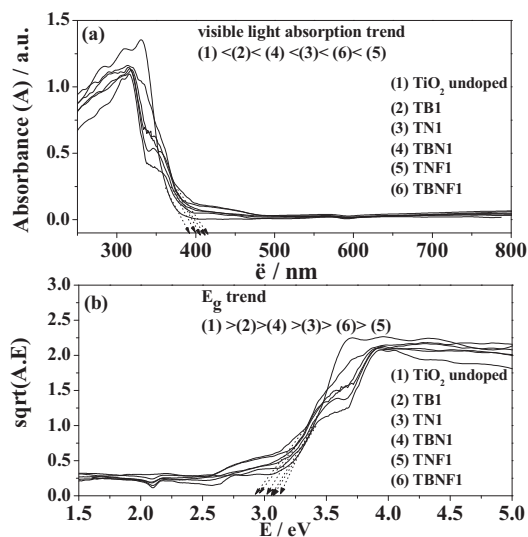


Fig. 2. (a) DR UV–vis spectra plots, (b) Kubelka Munk plots for all prepared B, N doped, B–N, N–F co-doped and B–N–F tri-doped TiO_2 catalysts. R: absorbance, $E = 1241.436 / \lambda$: energy in eV, λ : wavelength in nm.

21–1272). No rutile phase, potentially caused by boron doping [7] or B_2O_3 oxide impurities [6a,c], was detected. The present crystal phase results are in full agreement with the reports of Zhang et al. [21] and Ding et al. [22] which prepared B doped and B–N co-doped TiO_2 using H_3BO_3 as boron source.

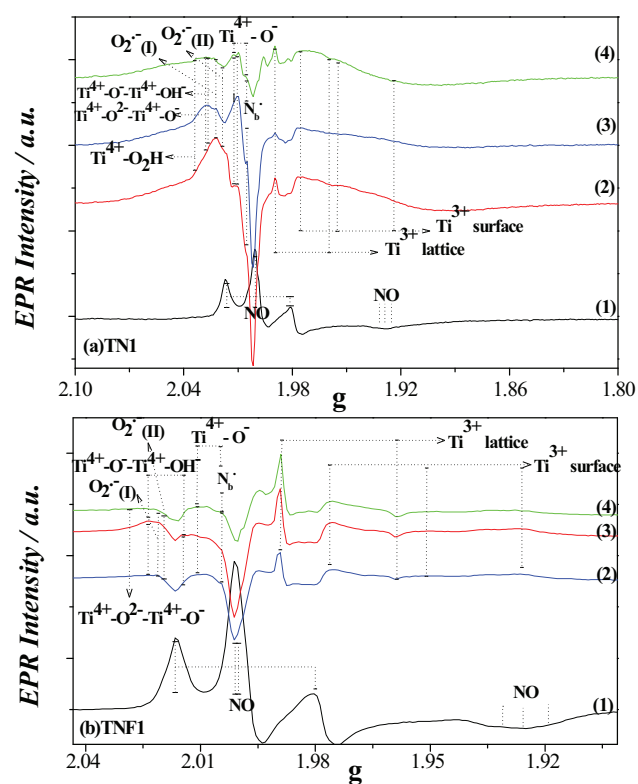


Fig. 3. EPR spectra of (a) TN1 and (b) TNF1 samples (1) at 77 K under dark, (2), UV–vis illumination conditions at 77 K under O_2 atmosphere, (3) visible light illumination conditions at 77 K under O_2 atmosphere, (4) illumination conditions at 77 K with isopropanol used as hole scavenger. Typical experimental conditions (1)–(4): amplifier, 1.552 mV, microwave power, 10 dB, sensitivity, 20 mV, time constant, 100 ms.

Using as starting model the obtained phase for each solid, a Rietveld refinement of the obtained XRD data was performed, based on the methodology developed in [31]. The refinement parameters included the obtained crystal phase, the cell parameters (a, c) and crystallite size are also included in Table 2. The difference between the experimental and theoretical patterns is displayed in the bottom of Fig. 1. The cell parameters (Table 2) for all prepared solids show a small difference in comparison with the theoretical values of pure TiO_2 anatase phase. Crystal lattice distortion is caused by the doping process [6,7,13,14,21] and this is known to be important for absorption–edge shift towards the visible-light region. Based on the line–width analysis of the anatase (101) diffraction peak, the average crystal sizes of all of these samples, estimated by the Scherrer equation, are summarized in Table 2. The estimated crystal sizes vary from 10.1 nm, 10.9 nm and 12.2 nm for TN1, TB1 and TBN1, to 13.3 nm and 14.6 nm for TBNF1 and TNF1 samples. In addition, the doping process decreases significantly the crystal size in all cases in comparison with undoped TiO_2 (21.0 nm). The results for TB1, TN1 and TBN1 samples are similar to those reported by Zhang et al. [21] who also observed a decrease in crystal size upon boron and nitrogen doping and co-doping. Boron and nitrogen doping can decrease the crystal size mainly due to the deformation of lattice and oxygen vacancies left by the substitution of O atoms by B or N atoms [21]. Chen et al. [6c], reported that boron doping inhibited grain growth that the average crystallite size for B– TiO_2 calculated at 500 °C decreased from 15 to 9, as the molar ratio of B to Ti (RB) increased from 0 to 20. On the other hand, Ding et al. [22] reported the increase of crystal size with boron and nitrogen doping. Ling et al. [27] also reported the increase of crystal size of obtained anatase crystal phase in B–N–F tri-doped prepared TiO_2

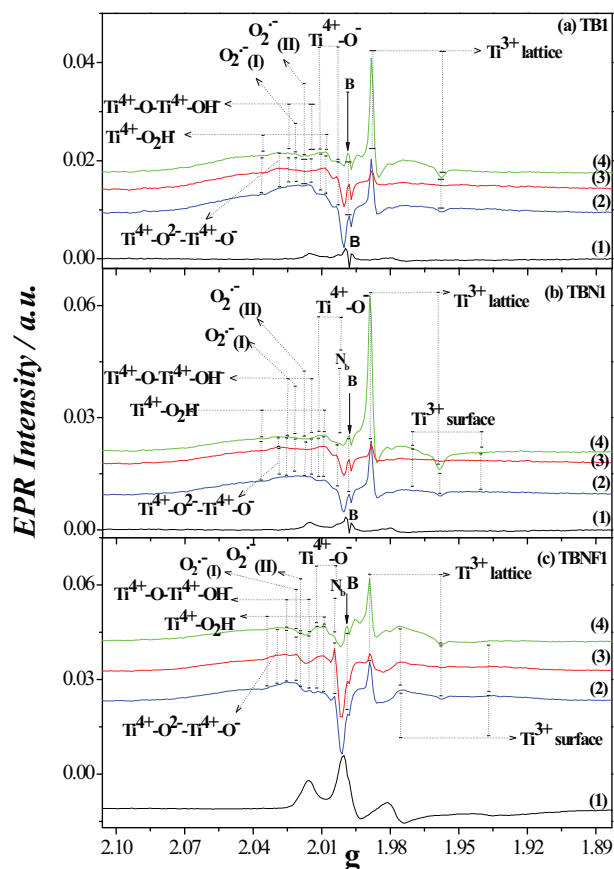


Fig. 4. EPR spectra of (a) TB1, (b) TBN1 and (c) TBNF1 samples (1) at 77 K under dark, (2), UV–vis illumination conditions at 77 K under O₂ atmosphere, (3) visible light illumination conditions at 77 K under O₂ atmosphere, (4) illumination conditions at 77 K with isopropanol used as hole scavenger. Typical experimental conditions (1)–(4): amplifier, 1.552 mV, microwave power, 10 dB, sensitivity, 20 mV, time constant, 100 ms.

samples caused probably by the ionic-liquid process used in their preparation.

3.2. UV–vis spectra

The DR UV–vis spectra plots of all doped, co-doped and tri-doped as prepared TiO₂ catalysts presented in Fig. 2a.

For the doped samples, the typical absorption edge i.e., due to electronic transitions from valence-band to conduction-band of TiO₂ is modified by the onset of a relatively broad absorption band in the visible region, whose intensity depends on the type of sample. This modification of absorption edge is lower for B, N doped, and B–N co-doped samples and more pronounced in the case of N–F co-doped and B–N–F tri-doped samples. The plots of transformed Kubelka–Munk function versus the energy of absorbed light, allow estimation of the band gaps (E_g), listed in Fig. 2b. The band gap energies are estimated to be 3.08, 3.01, 3.04, 2.91 and 2.94 eV for TB1, TN1, TBN1, TNF1 and TBNF1 catalysts correspondingly, while for the undoped TiO₂ sample E_g = 3.18 eV. Accordingly, it could be stated that: [i] all doped samples have smaller band gap E_g than undoped TiO₂, [ii] concomitant presence of N and F ions in TNF1 and TBNF1 samples causes a more intense decrease of E_g than B and N ions in TB1, TN1 and TBN1 samples, [iii] TBN1 and TBNF1 have lower E_g values than mono doped TB1 but higher than TN1 and TNF1.

The observation that samples co-doped with N–F (TNF1, TBNF1) provide a higher visible light absorption than samples doped with

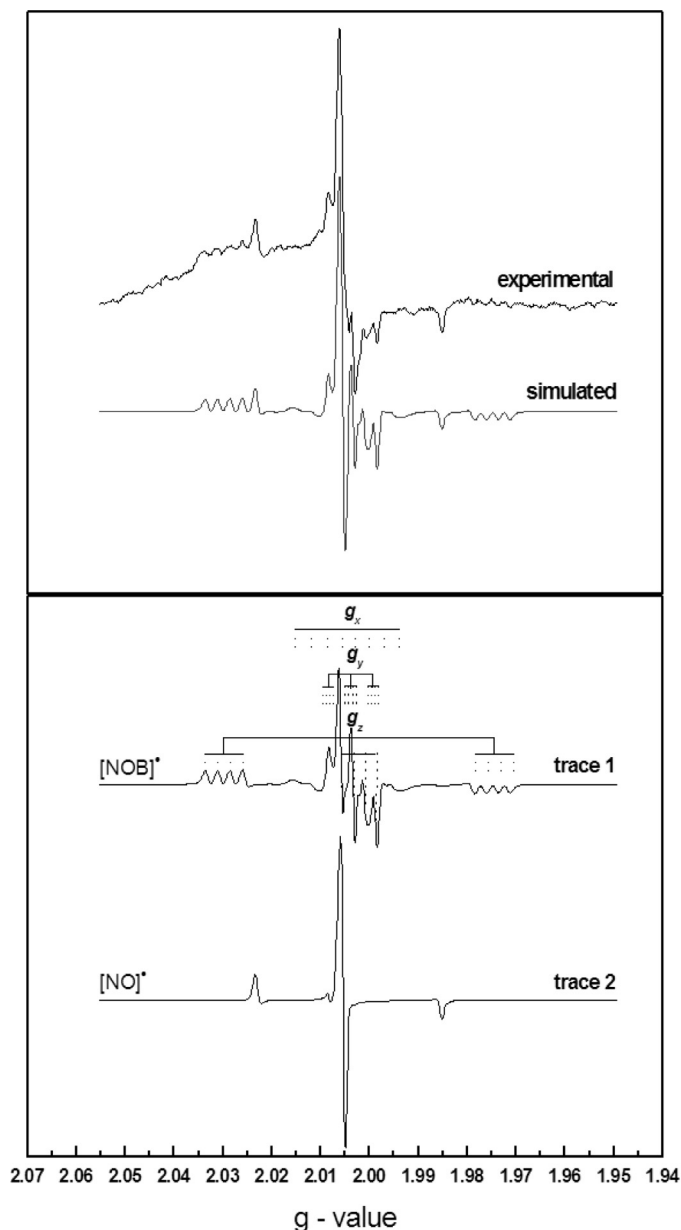


Fig. 5. Room temperature EPR spectrum of TBN1 sample (experimental) along with computer simulated spectrum (theoretical). Trace 1 and 2 are the traces of the two species introduced in the computation which determine the theoretical spectrum. Instrument settings: microwave frequency 9.51 GHz, microwave power: 3.1 mW, modulation amplitude: 4 G.

N ions (TN1, TBN1) is in agreement with our previous work [13]. It has been reported [13,18] that F ions help the incorporation of N ions in the bulk of anatase crystal, thus creating impurity states which cause the visible light absorption phenomena. The present results for TB1, TN1 and TBN1 samples agree with the data previously reported by Wu et al. [20] who used a similar sol–gel route as we did here i.e., H₃BO₃ as boron ion source, urea as N source and TTIP as Ti source. In [20] they measured lower E_g values of for B–N–TiO₂ (2.13 eV) than N–TiO₂ (2.16 eV). Ding et al. [22] also used H₃BO₃ as boron source, urea as nitrogen source and TiCl₄ as titanium source for the synthesis of B doped, N doped and B,N co-doped TiO₂ applied for NO removal and reports E_g values very close to our values with the same trend: N doped (2.66 eV) < B,N co-doped (2.77 eV) < B doped (3.03 eV). In et al. [19] used a different experimental procedure i.e., TiCl₄ as Ti source and BH₃ as boron ion source,

Table 4

Spin Hamiltonian parameters g , A used for the theoretical simulation of the EPR spectrum of TBN1 at room temperature.

	g -values			A -values					
	g_x	g_y	g_z	$A(^{14}\text{N})$ Gauss			$A(^{11}\text{B})$ Gauss		
				A_x	A_y	A_z	A_x	A_y	A_z
$[\text{NO}]^{\bullet}$	2.006	2.005	2.004	2	3.1	32	–	–	–
$[\text{NOB}]^{\bullet}$	2.004	2.003	2.001	9.3	10	50	4.8	0.7	4.5

however they reported DR UV–vis spectra plots comparable to our data (Fig. 2) for N doped and B–N co-doped TiO_2 while their E_g values for B- TiO_2 were higher than E_g for N- TiO_2 and B–N- TiO_2 [19].

3.3. Surface area and porosity

From the adsorption–desorption isotherms and the calculated values of specific surface area (S_p), pore volume (V_p) and mean pore diameter (D_{mean}) listed in Table 2, it is concluded that all prepared samples are typical mesoporous materials. These mesopores should be formed by the agglomeration of TiO_2 nanocrystals [22]. Based on the values included in Table 2 it can be noted: [i] Boron and nitrogen incorporation lead to an increase of S_p and V_p values and decrease of the D_{mean} values; [ii] F incorporation decreases S_p , V_p values and enhance D_{mean} values; and [iii] incorporation of boron and nitrogen leads to the highest surface area values. Thus, both B–N co-doped and B–N–F tri-doped TiO_2 samples have higher S_p values than N-doped and N–F co-doped samples, correspondingly. In addition, the S_p of B-doped sample is also higher than undoped sample ones while N–F co-doped sample has the lowest S_p value and the highest D_{mean} value. The increase of BET surface area when B and N ion added is in agreement with previous reports [21,22,27]. Ding et al. [22] also reported that the presence of H_3BO_3 could significantly enhance the surface area of the sample while B and N addition gave also higher S_p values than boron mono-doped samples. This increment in S_p values and decrease in D_{mean} values for B-doped and B–N-doped samples could be beneficial for their photocatalytic efficiency compared with the photocatalysts with no boron doping.

3.4. EPR study

Fig. 3 and Fig. 4 display low temperature EPR spectra for N-containing samples (TN1 and TNF1 Fig. 3) and boron-containing samples TB1, TBN1 and TBNF1 (Fig. 4). The g - and ^{14}N ($I=1$) hyperfine-tensors for all paramagnetic species detected by EPR are listed in Table 3. The EPR spectra for the TB1 and TBN1 samples are analyzed in detail in Fig. 5, and the derived parameters for the B-atoms are listed in Table 4.

In Fig. 4, using the g - and A -tensors from Table 3, the structural assignment of these centers was done according to previous reports of Valentin et al. [18], Li et al. [32], Berger et al. [33], Coronado et al. [34], Livraghi et al. [35] and Fittipaldi et al. [36]. In Fig. 3 the EPR spectra for TN1 (Fig. 3a) and TNF1 (Fig. 3b) samples – without boron doping – are presented.

3.4.1. Nitrogen and nitrogen–fluorine doping

In accordance with our previous reports [13,14] N-doping creates two kinds of paramagnetic species. [a] Non-photoactive NO species which are located in the surface and [b] photoactive N_b^{\bullet} species [17,18] which are bonded in the bulk of TiO_2 crystal. Two types of localized energy states in N- TiO_2 have been proposed on the basis of experimental evidences [17,35] and rigorous quantum chemical calculation [17]. They are associated to two different

nitrogen bulk species, namely substitutional N atoms (N_s), where nitrogen substitutes O lattice ions, and interstitial N atoms (N_i), where N binds to O lattice ions. So, in the dark (Fig. 3; lines denoted as (1)), the g_1 (2.001), g_2 (1.998), g_3 (1.927) [17,13] components of NO species can be resolved with a ^{14}N -hyperfine splitting tensor $A(^{14}\text{N})=[A_1<1\text{G}, A_2=32.2\text{G}, A_3=9.6\text{G}]$, respectively. In dark the NO signal overwhelmed the weak g_1 (2.005) signal of N_b^{\bullet} species [13,17,18,35].

In addition, N atom insertion in the TiO_2 crystal creates two kinds of Ti^{3+} ions [13,14,18] which are photoinduced as observed in the EPR spectra under UV–vis illumination (Fig. 3a, b; lines denoted (2)). The broad signals with $g_1 = 1.972$, $g_2 = 1.954$ and $g_3 = 1.93$ correspond to Ti^{3+} ions formed on the surface of the particle [14,37], while the sharp signals with $g_1 = 1.989$ and $g_2 = 1.964$ correspond to Ti^{3+} ions formed in the lattice of TiO_2 . As observed in Fig. 3 the ratio of lattice Ti^{3+} to surface Ti^{3+} are lower in TN1 and higher in TNF1 sample. This happens because F ions enhance the insertion of N atoms deeper in the anatase lattice and favors the formation of more Ti^{3+} lattice states as shown previously [13,18,38].

In Fig. 3 (lines denoted as (2)), except of the enhancement of EPR signals of photoinduced N_b^{\bullet} species ($g_1 = 2.005$) and Ti^{3+} surface and lattice ions, UV–vis triggers the generation of two $\text{O}_2^{\bullet-}$ type signals with g_{zz} components at 2.021 and 2.0184 [14,34,35] which are more intense in TN1 sample. In addition, under O_2 atmosphere and UV–vis illumination two other kinds of oxygen related signals are observed. The first signal with $g_1 = 2.0046$, $g_{\perp} = 2.0121$ is attributed to $[\text{Ti}^{4+}-\text{O}^-]$ trapped holes which are produced by the reaction of anatase holes with lattice oxygen according to Berger et al. [33]. According to newest reports [27,39,40] the same signal ($g_1 = 2.0046$, $g_{\perp} = 2.0121$) is named as OV_s and it is created by the insertion of nitrogen into anatase crystal lattice [39,40]. The second signal is attributed to $[\text{Ti}^{4+}-\text{O}^{2-}-\text{Ti}^{4+}-\text{O}^-]$ according to Berger et al. [33] with g_{zz} component at 2.028. Also weak signals of $\text{Ti}^{4+}-\text{O}_2\text{H}$ ($g_{zz} = 2.034$, $g_{yy} = 2.009$) [34] in TN1, and $\text{Ti}^{4+}-\text{O}^- - \text{Ti}^{4+}-\text{OH}^-$ ($g_{zz} = 2.024$, $g_{yy} = 2.014$) [35] in both TN1 and TNF1 samples, have been observed in the left part of the EPR spectrum [34] corresponding to ($\bullet\text{O}_2\text{H}$, $\bullet\text{OH}$) radicals [32–35].

Under visible light ($\lambda > 400$ nm) illumination (Fig. 3a, b; lines denoted as (3)) an increase in the components of $\text{Ti}^{4+}-\text{O}^-$ OV_s and $\text{O}_2^{\bullet-}$ radicals is observed in both TN1 and TNF1 samples. In the case of TNF1 a small increase of Ti^{3+} lattice signal at $g_1 = 1.989$ is denoted.

When isopropanol was used as hole scavenger (Fig. 3a, b; lines denoted as (4)) an attenuation or disappearance of the $g_1 = 2.005$ N_b^{\bullet} species' component is observed. As reported previously [14] this indicates that N_b^{\bullet} species react as holes in N-doped TiO_2 . In the same spectrum a more pronounced enhancement of both Ti^{3+} lattice and surface ions is observed in the presence of isopropanol which indicates that such species supports electron photogeneration mechanism in TN1 and TNF1 samples [13,14,38].

3.4.2. Boron-doping

In Fig. 4 the EPR spectra of boron containing samples TB1, TBN1 and TBNF1 are presented. At a first glance it is obvious that the main differences in the EPR spectra between the boron containing samples in Fig. 4 and the EPR spectra of TN1 and TNF1 samples in Fig. 3, are: [a] the presence of higher quantities of $\bullet\text{O}_2\text{H}$ and $\bullet\text{OH}$ in the left part of spectra, [b] the more intense signal of $\text{Ti}^{4+}-\text{O}^-$ OV_s in the middle part of spectra and [c] the stronger induction of Ti^{3+} lattice centers at $g = 1.989$ ions in the right part of spectra for TBN1 sample in comparison with TN1 sample. Let us start the assignment from the single boron doped sample TB1 in Fig. 4a which is also quite the same for TBN1 (Fig. 4b) and TBNF1 (Fig. 4c) samples. Under UV–vis irradiation (Fig. 4a; line (2)) in the right part of spectra the g component of Ti^{3+} lattice ions is clearly resolved at 1.989 while no Ti^{3+} surface ions are detected. This component of lattice Ti^{3+} is

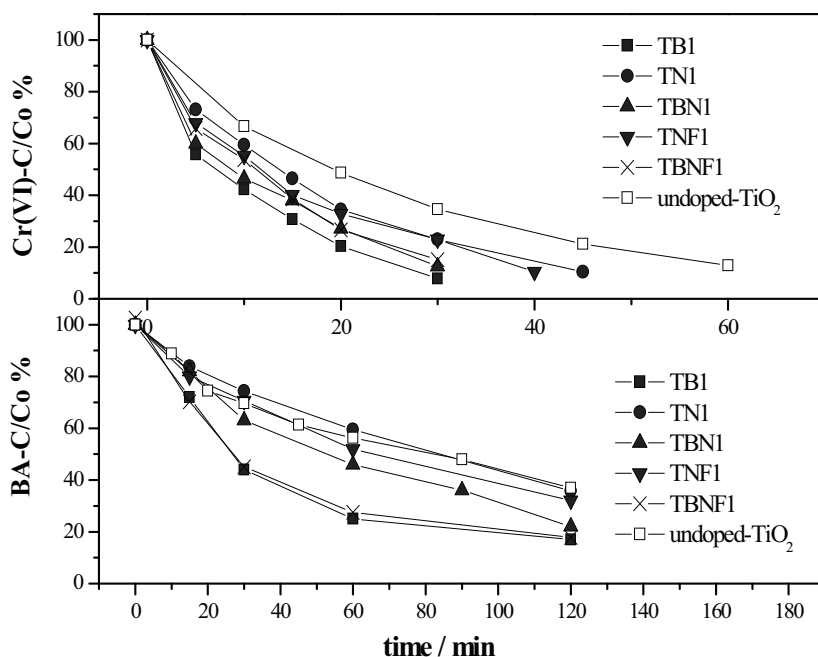


Fig. 6. Time profile of (a) Cr(VI) reduction and (b) benzoic acid oxidation for all B, N doped, B–N, N–F co-doped and B–N–F tri-doped TiO₂ catalysts in comparison with undoped TiO₂ sample under UV–vis irradiation. Initial concentrations of Cr(VI) = 0.05 mM and benzoic acid = 0.01 mM; 500 mg L^{−1} catalyst; pH 2, under air conditions.

less prominent under visible light irradiation (see line (3)), while it is stronger when isopropanol was used as hole scavenger (line (4)).

In the left part of spectrum under UV–vis irradiation in O₂ atmosphere (Fig. 4a; line (2)) the components of two types of O₂^{•−} radicals (2.021, 2.0184), Ti⁴⁺–O[−] OV (2.0046) and Ti⁴⁺–O^{2−}–Ti⁴⁺–O[−] (2.028) are resolved as in the case of TN1 and TNF1 samples. Moreover in the case of TB1 sample, the $g = 2.024$ component of Ti⁴⁺–O[−]–Ti⁴⁺–OH[−] and $g = 2.034$ of Ti⁴⁺–O₂H are clearly resolved, while the $|g| = 2.0046$ component of Ti⁴⁺–O[−] OV is more intense.

Under visible light illumination (line (3)) the spectral features remain the same, however with much lower intensity than spectra under UV–vis irradiation (line (2)) a fact revealing lower visible light activity of the TB1 material.

In Fig. 4b the EPR spectra of TBN1 samples are quite comparable to those for the TB1. Ti³⁺ lattice and surface ions are presented in the right part of spectrums while O₂^{•−}, •OH and •O₂H radicals in the left part. In comparison with TN1 (Fig. 3a) it was observed that boron incorporation enhances the Ti³⁺ lattice centers and decreases Ti³⁺ surface centers with a concomitant enhancement in •OH, •O₂H radicals and Ti⁴⁺–O[−] OV.

Fig. 5 shows a numerical simulation of the boron EPR signals in the TBN1 material. Previously, Czoska et al. [24] and Fittipaldi et al. [36] have shown that in B–N co-doped TiO₂ a new paramagnetic specie can be detected containing both B and N atoms in interstitial bonding with the same lattice oxygen atom and labeled as [NOB][•] [24]. In our TBN1 material this specie can be resolved in room temperature (see in Fig. 5). The signal has been simulated assuming an electron coupled with one ¹⁴N($I = 1$) nucleus plus a ¹¹B($I = 3/2$) nucleus (see simulated spectra in Fig. 5A and B). The derived spin Hamiltonian parameters listed in Table 4 are comparable with those originally reported by Czoska et al. [24]. Finazzi et al. [8] have studied the B–TiO₂ material with density functional theory and proposed that boron could occupy either a substitutional oxygen-site or interstitial to oxygen atoms in the bulk of anatase. Boron substitutional to oxygen results in a paramagnetic defect [8,24], [BTi₃], which introduces new states in the midgap of the material and causes red shift in the adsorption spectra [8].

Boron in interstitial positions, with oxygen atoms [BO₃] behaves as a three-electron donor [8] with formation of B³⁺ and reduction of Ti⁴⁺ to Ti³⁺ according to equation: $B + 3Ti^{4+} \rightarrow B^{3+} + 3Ti^{3+}$ [8]. The paramagnetic [BTi₃] could easily trap electrons from other defect states (e.g., Ti³⁺ ions) and convert into the EPR-silent [BTi₃][−] species [8,24]. Overall in our case the detection of [NOB] species, the presence of high amount of Ti³⁺ lattice ions ($g = 1.989$) and the small narrowing of band gap energy of TB1 sample (see Table 2) leads to the conclusion that boron ion probably exist in interstitial position with oxygen atoms of anatase lattice but it is not impossible the existence of lower amounts of substitutional boron states.

In Fig. 4c the EPR spectra of TBNF1 samples looks like a mixed spectra of TB1 and TNF1 samples (Fig. 3b). As it is also noticed above for TB1 and TBN1 samples boron incorporation in the case of TBNF1 sample also enhances •OH, •O₂H radicals while reduces Ti³⁺ lattice and surface centers in comparison with TNF1 sample (Fig. 3). To support our conclusions the EPR intensity values of •OH, •O₂H radicals ($I_{Ti^{4+}-O^{-}-Ti^{4+}-OH^{-}} g = 2.024$, $I_{Ti^{4+}-O_{2}H} g = 2.035$), Ti⁴⁺–O[−] OV (I_{Ti⁴⁺–O[−]}, $|g| = 2.0046$), Ti³⁺ lattice and surface ions ($I_{Ti^{3+} \text{ lattice}} g = 1.989$, $I_{Ti^{3+} \text{ surface}} g = 1.972$) photogenerated species are summarized in Table 5.

Overall, the present EPR experiments provided a wealth of information that can be recapitalized as follows:

1. Samples TN1 and TNF1 without boron: Both TN1 and TNF1 samples contain N_b[•] photoexcited species and two kinds of Ti³⁺ electrons e.g., lattice and surface. More lattice Ti³⁺ electrons, are photogenerated in TNF1 while more surface Ti³⁺ electrons are photogenerated in TN1. In both TN1 and TNF1 O₂^{•−} radicals and OV (Ti⁴⁺–O[−]) are photogenerated, while less •OH, •O₂H radicals are detected. Finally, in both TN1 and TNF1 visible light illumination has significant contribution in the photoexcitation of the above denoted species while the use of isopropanol increases the Ti³⁺ electrons lifetime acting as hole scavenger.
2. Boron-doped TB1, TBN1 and TBNF1: Boron incorporation in the anatase lattice: [i] increases the lattice Ti³⁺ electrons formation in TB1 and TBN1 samples through the route (1):

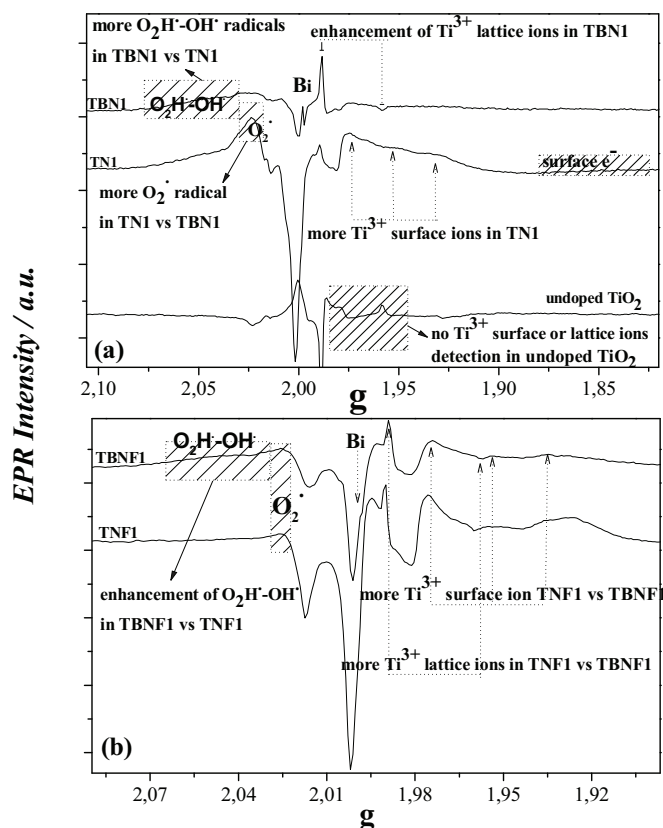
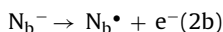
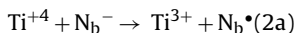
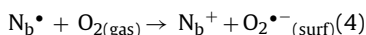
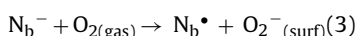


Fig. 7. UV-vis light-minus-dark plots for (a) undoped TiO₂, TN1 and TBN1 sample (b) TNF1 and TBNF1 sample.

reduction of electron-hole pair recombination rate. In addition, N insertion in the anatase lattice forms the N_b^\bullet species which increase the energy state of the valence band E_{VB} level [13,14,17,18,41]. These N_b^\bullet species can act as electron transfer centers supporting the reduction mechanism via two different paths [35]:



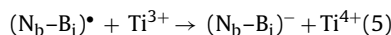
Mechanism (2a) is prevalent when lattice Ti^{3+} defects are formed because of the deeper insertion of N atoms assisted by F ions (i.e., in TNF1) [13,17,41], while mechanism (2b) is prevalent when N insertion it is not so deep in the lattice [13] and photoexcited electrons captured by surface Ti^{4+} and creates surface Ti^{3+} defects (i.e., in TN1). These photoexcited electrons are clearly detected in the end of TN1 EPR signal (see Fig. 7a) as reported before [14] and causes the more intense signals of $O_2^{\bullet-}$ radicals through the reaction: $e^- + O_2 \rightarrow O_2^{\bullet-}$ [27]. In the case of TNF1 catalyst these surface electrons disappeared because are trapped by F ions adsorbed in the surface in the case of TNF1 sample [27]. N_b^\bullet species can also support the oxidation mechanism through the routes [35]:



Thus, we conclude that the observed higher photocatalytic activity achieved by TN1 and TNF1 materials versus undoped TiO₂ in simultaneous benzoic acid oxidation and Cr(VI) reduction, can be attributed to the N_b^\bullet species, $O_2^{\bullet-}$ and surfacial Ti^{3+} electrons, respectively.

3.5.1.2. B-N co-doped and B-N-F tri-doped samples vs N-doped and N-F co-doped. The enhanced photocatalytic activity of B-N co-doped and B-N-F tri-doped TiO₂ versus N-doped and N-F doped TiO₂ catalysts have been also investigated in previous reports [22,27]. Ding et al. [22] used the same boron source (H_3BO_3) as we did here to prepare B-N co-doped, B-doped and N-doped TiO₂. They have reported [22] similar decrease of E_g values for B, N doped and B-N co-doped samples, as we do here. They have also detected Ti^{3+} centers with XPS measurements and measured higher photocatalytic activity of B-N sample in the removal of NO. They [22] proposed that Ti^{3+} electrons lead to the formation of the defects (e.g., oxygen vacancies) and enhance the final photocatalytic activity while the charge compensation between B (3+) and N (1-) through an internal charge transfer with a large stabilization effect in the B-N co-doped TiO₂ largely reduced the photo transition energy from the valence band to the conduction band, resulting in a higher photocatalytic activity [18].

Czoska et al. [24] has been reported that the energy level of the $(N_b-B_i)^\bullet$ species is located close to the edge of the valence band and lies below the corresponding level of N_b^\bullet . This $(N_b-B_i)^\bullet$ center turns out to be a good electron acceptor leading to the formation of diamagnetic $(N_b-B_i)^-$ species [24]. A possible route for this electron transfer could be through the Ti^{3+} states induced by the B and N doping according to:



Herein, we propose two different cases for the B-N co-doped sample and B-N-F tri doped sample, correspondingly: [a] detection of higher amounts of lattice Ti^{3+} ions in TBN1 than in TN1 sample (see Fig. 7a and Table 5) leads to the enhancement of mechanism (2a) with mechanisms (1) and the increment of the reduction ability; [b] in a second less possible case TBN1 sample follows the mechanism (5). If this was the case it should be detected less Ti^{3+} signals. Thus, our findings show that Ti^{3+} signals are more in TBN1 sample than TN1 (see Fig. 7a and Table 5) making more possible the first case. On the other hand TBNF1 sample has more Ti^{3+} lattice ions than TB1 but less than TNF1 sample (see Fig. 7b and Table 5). So, mechanism (5) seems more possible to take also place for TBNF1 sample.

In Fig. 7a, it is obvious that the amounts of secondary $\bullet OH$, $\bullet O_2H$ radicals and $Ti^{4+}-O^-$ OV are much higher in TBN1 and TBNF1 than in TN1 and TNF1 (see also Table 5). This explains the observation that the benzoic acid oxidation by TBN1 and TBNF1 catalysts is more efficient than by TN1 and TNF1. As it is noticed in our previous report, the photocatalytic degradation pathway for benzoic acid oxidation proceeds mainly via $\bullet OH$ attack on the aromatic moiety on several positions to produce hydroxy and dihydroxy derivatives and also via decarboxylation (photo-Kolbe) reaction resulting from the direct attack of the carboxylic group by h^+_{VB} [42,43]. Finally, the higher S_p values and lower D_{mean} values of both TBN1 and TBNF1 sample in comparison with TN1 and TNF1 samples correspondingly supports the photocatalytic superiority of TBN1 and TBNF1 samples vs TN1 and TNF1 samples.

Li et al. [27] also prepared B-N-F tri-doped TiO₂ and also obtained higher photocatalytic activity for degradation of methyl orange. This higher photoactivity was attributed to the presence of a Ti-B-N structure on the TiO₂ surface and a synergistic effects of N, B and F, which improve the electron/hole separation efficiency. EPR was also used for the characterization of B-N-F tri-doped catalysts in their study and they reported also the detection of enhanced Ti^{3+} , OV and $\bullet OH$ signals. In their analysis [27] they proposed that F ions may have a special role in the synergistic effect of B-N-F tri-doping. Fluorine – as the most electronegative element – can be adsorbed in the surface of TiO₂ and can attract photo-generated electrons, and thus causes an extra slowing in the recombination

rate of the photo-generated electrons and holes, and thus improve the photocatalytic activity [44].

3.5.1.3. B-doped vs B–N co-doped and B–N–F tri doped TiO_2 . Based on the Cr(VI) reduction and BA oxidation rates (Table 5) single boron doped TiO_2 has the highest photocatalytic activity. This result looks strange at first because TB1 sample exhibited higher E_g value (3.08 eV) than TBN1 (3.06 eV) and TBNF1 (2.94 eV) samples. Liu et al. [45] reported higher photocatalytic activity of B–N co-doped vs singly B-doped TiO_2 when hydrothermal process is followed for the preparation of the catalysts due to the formation of O–Ti–B–N structure that facilitates the separation and transfer of charge carriers, while the opposite trend is expected with sol gel method as in our case.

On the other hand, higher photocatalytic activity of TB1 sample than TBN1 and TBNF1 is in full agreement with our EPR findings. The intensity values trend of $\text{Ti}^{4+}\text{--O}^-$ ($g=2.0046$) OVs (Table 5) created by the insertion of dopant in the crystal lattice [27,39,40] are in agreement with Cr(VI) reduction rate. Single boron doping creates higher amounts of OVs in anatase TiO_2 lattice than B–N co-doping and B–N–F tri-doping. Wu et al. [46] found also that B doping lead to an increase in the formation of OVs [27]. Recent EPR studies in N-doped TiO_2 [39,40] have been shown that OVs can capture photogenerated electrons from the bulk, facilitating the redox reactions. Since B^{3+} doping in TiO_2 lattice was electron-deficient, it could act as a shallow trap for electrons, thus prolonging the life of photoinduced electrons and holes and enhancing the activities of the catalysts [47]. Finally, boron incorporation in anatase crystal creates the highest amounts of secondary $\cdot\text{OH}$, $\cdot\text{O}_2\text{H}$ radicals than TBN1 and TBNF1 samples and this is in full agreement with the higher BA oxidation rates of TB1 sample compared to TBN1 and TBNF1 catalysts, as denoted also in Table 5.

3.5.2. Photocatalytic kinetics under visible light irradiation

Fig. 8 shows the kinetic profiles for the simultaneous Cr(VI) reduction (upper part) and benzoic acid oxidation (lower part), at pH 2 under visible irradiation for all prepared catalysts.

According to the observed kinetics (Fig. 8) undoped TiO_2 is inactive under visible light irradiation i.e., as expected taking into account the E_g value. In addition, higher oxidation than reduction rates were observed for all doped catalysts, that is the inverse trend compared with that observed under UV–vis irradiation. Overall, the activity towards photocatalytic Cr(VI) reduction and BA oxidation under visible light irradiation follows the same trend:

Cr(VI) reduction and BA oxidation:
TNF1 > TBNF1 > TN1 > TBN1 > TB1

At first glance, the above efficiency trend coincides with that of the E_g trend of all prepared catalysts. In other words as the E_g values of obtained doped TiO_2 catalysts decrease, the photoredox efficiency under visible light irradiation increases, as expected. Thus, as the absorption edge of the photocatalysts increased, more $\text{h}^+\text{--e}^-$ pairs were photogenerated leading to an increase Cr(VI) reduction and BA oxidation ability. As it was already discussed, the increase of adsorption edge in the visible light region is higher for N/F containing samples (TNF1, TBNF1), less for N containing ones (TN1, TBN1) and least for B doped sample (TB1).

This observed kinetics were also supported by the EPR data. In Fig. 9 the [visible light irradiated] minus [dark] signals are plotted for all catalysts. As shown in the left part of plots the total amount of photoexcited Ti^{3+} surface and lattice ions (e^- signals) under visible light follow the same trend with the Cr(VI) reduction rates. This result indicates that Ti^{3+} states formed on the surface and in the bulk of anatase crystal, enhance visible light adsorption edge and directly enhance the Cr(VI) reduction. Finally, as discussed previously in Figs. 3 and 4 (signals labeled as (3) in both figures) an increase in $\text{N}_\text{b}\cdot$, $\text{Ti}^{4+}\text{--O}^-$ OVs and $\text{O}_2\cdot^-$ radicals is observed in

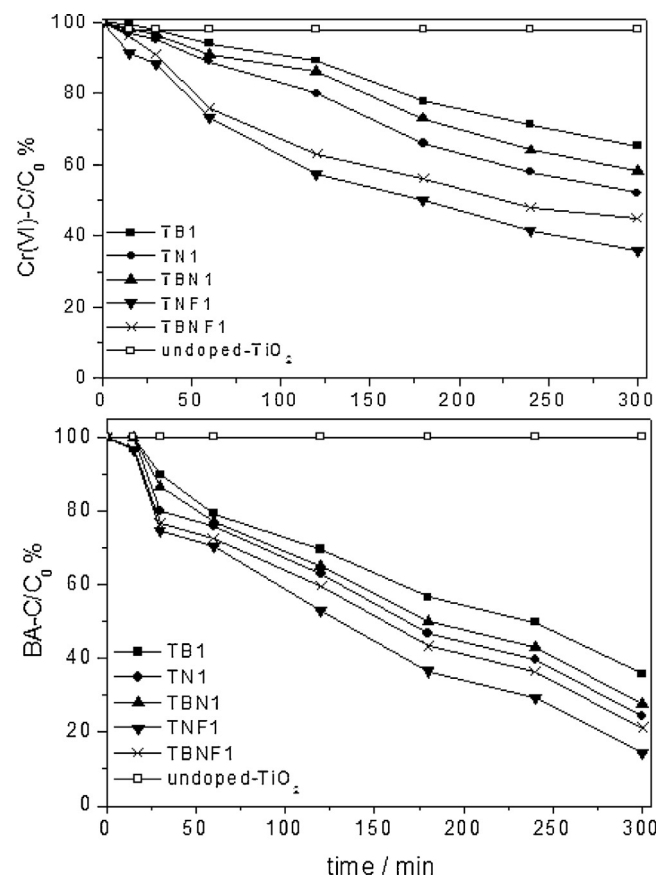


Fig. 8. Time profile of (a) Cr(VI) reduction and (b) benzoic acid oxidation for all B, N doped, B–N, N–F co-doped and B–N–F tri-doped TiO_2 catalysts in comparison with undoped TiO_2 sample. Initial concentrations of Cr(VI) = 0.05 mM and benzoic acid = 0.01 mM; 500 mg L^{-1} catalyst; pH 2, under air conditions.

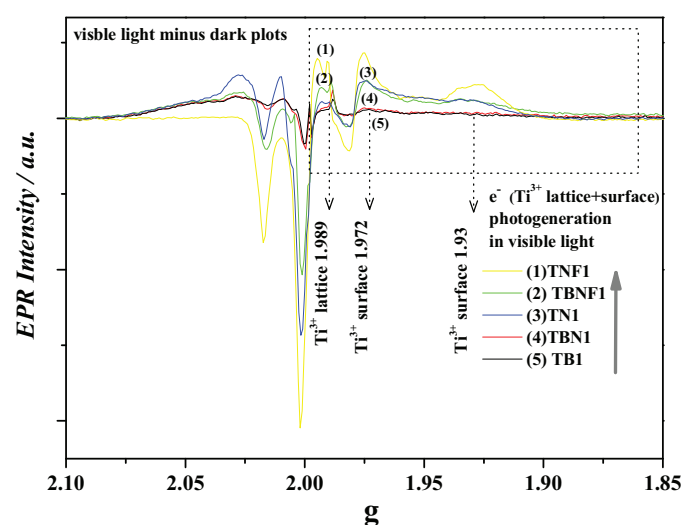


Fig. 9. Visible light–minus–dark plots for TNF1, TN1, TBNF1, TBN1 and TB1 catalysts samples.

both TNF1 and TN1 samples. On the contrary, in B-doped materials visible light photoexcitation is suppressed, i.e., the corresponding signals showed lower intensities.

4. Conclusions

B-doped, B–N co-doped and B–N–F tri-doped TiO₂ photocatalysts prepared by sol–gel method have been characterized and applied for the simultaneous reduction of Cr(VI) and oxidation of benzoic acid. N doped, N–F co-doped and undoped TiO₂ catalysts also prepared via the same method as blank samples. Anatase phase with tetragonal I41 space-group was formed in all cases. A narrowing of E_g values for all doped catalysts was observed while F doping reduces more the E_g values. EPR study showed: [i] the formation of N_b species, Ti⁴⁺–O[–] OV and Ti³⁺ surface and lattice ions in N and N–F doped samples; [ii] Boron ions incorporation in interstitial positions creates more Ti⁴⁺–O[–] OV and supports oxidation mechanism through the formation of secondary •OH, •O₂H radicals while creates new states above valence band and slightly below N states.

Photocatalytic experiments under UV–vis light irradiation for the simultaneous Cr(VI) reduction and BA oxidation showed: [i] an increase of reduction and oxidation rates of N doped and N–F co-doped samples in comparison with the undoped one that is explained by the Ti³⁺ states and the visible light improvement by N states' insertion; [ii] the enhancement of redox rates of B–N co-doped and B–N–F tri-doped samples versus N-doped and N–F co-doped materials, which was attributed to the enhancement of OH O₂H radicals' yield and reduced electron/hole recombination rate, due to Ti³⁺ lattice defects' increase; [iii] higher photoactivity of B-doped catalyst due to higher lattice distortion caused by boron insertion and the increased formation of Ti⁴⁺–O[–] OV and OH, O₂H radicals. On the contrary, under visible light irradiation photoexcitation of B-doped catalysts is suppressed and the catalytic efficiency of both Cr(VI) reduction and BA oxidation followed the trend of E_g increase.

References

- [1] M. Anpo, M. Takeuchi, *J. Catal.* 216 (2003) 505–516.
- [2] I.K. Konstantinou, T.A. Albanis, *Appl. Catal. B: Environ.* 42 (2003) 319–335.
- [3] S. Banerjee, S.C. Pillai, P. Falaras, K.E. O'shea, J.A. Byrne, D.D. Dionysiou, *J. Phys. Chem. Lett.* (2014) 2543–2554.
- [4] R. Asahi, T. Morikawa, T. Ohwaki, K. Aoki, Y. Taga, *Science* 293 (2001) 269–271.
- [5] L. Gomathi Devi, R. Kavitha, *Appl. Catal. B: Environ.* 140–141 (2013) 559–587.
- [6] (a) A. Zaleska, J.W. Sobczak, E. Grabowska, J. Hupka, *Appl. Catal. B Environ.* 78 (2008) 92–100; (b) A. Zaleska, E. Grabowska, J.W. Sobczak, M. Gazda, J. Hupka, *Appl. Catal. B Environ.* 89 (2009) 469–475; (c) D. Chen, D. Yang, Q. Wang, Z. Jiang, *Ind. Eng. Chem. Res.* 45 (2006) 4110–4116.
- [7] N. Lu, H.M. Zhao, J.Y. Li, X. Quan, S. Chen, *Sep. Purif. Technol.* 62 (2008) 668–673.
- [8] E. Finazzi, C. Di Valentin, G. Pacchioni, *J. Phys. Chem. C* 113 (2009) 220–228.
- [9] B. Zhou, M. Schulz, H.Y. Lin, S. Ismat Shah, J. Qu, C.P. Huang, *Appl. Catal. B: Environ.* 92 (2009) 41–49.
- [10] Q. Xiang, J. Yu, W. Wang, M. Jaroniec, *Chem. Commun.* 47 (2011) 6906–6908.
- [11] M.R. Bayati, A.Z. Moshfegh, F. Golestani-Fard, *Appl. Catal. A Gen.* 389 (2010) 60–67.
- [12] S. Tosoni, O. Lamiel-Garcia, D. Fernandez Hevia, J.M. Doña, F. Illas, *J. Phys. Chem. C* 116 (2012) 12738–12746.
- [13] A.E. Giannakas, E. Seristatidou, Y. Deligiannakis, I. Konstantinou, *Appl. Catal. B: Environ.* 132–133 (2013) 460–468.
- [14] A.E. Giannakas, M. Antonopoulou, Y. Deligiannakis, I. Konstantinou, *Appl. Catal. B: Environ.* 140–141 (2013) 636–645.
- [15] Q. Xiang, J. Yu, M. Jaroniec, *Phys. Chem. Chem. Phys.* 13 (2011) 4853–4861.
- [16] J. Xu, B. Yang, M. Wu, Z. Fu, Y. Lv, Y. Zhao, *J. Phys. Chem. C* 114 (2010) 15251–15259.
- [17] F. Napoli, M. Chiesa, S. Livraghi, E. Giamello, S. Agnoli, G. Granozzi, G. Pacchioni, C. Di Valentin, *Chem. Phys. Lett.* 477 (2009) 135–138.
- [18] C. Di Valentin, E. Finazzi, G. Pacchioni, S. Livraghi, A.M. Czoska, M.C. Paganini, E. Giamello, *Chem. Mater.* 20 (2008) 3706–3714.
- [19] S. In, A. Orlov, R. Berg, F. García, S. Pedrosa-Jimenez, M.S. Tikhov, D.S. Wright, R.M. Lambert, *J. Am. Chem. Soc.* 129 (2007) 13790–13791.
- [20] G. Wu, J. Wen, J. Wang, D.F. Thomas, A. Chen, *Mater. Lett.* 64 (2010) 1728–1731.
- [21] K. Zhang, X. Wang, T. He, X. Guo, Y. Feng, *Powder Technol.* 253 (2014) 608–613.
- [22] X. Ding, X. Song, P. Li, Z. Ai, L. Zhang, *J. Hazard. Mater.* 190 (2011) 604–612.
- [23] N.O. Gopal, H.-H. Lo, S.-C. Ke, *J. Am. Chem. Soc.* 130 (2008) 2760–2761.
- [24] A.M. Czoska, S. Livraghi, M.C. Paganini, E. Giamello, C. Di Valentin, G. Pacchioni, *Phys. Chem. Chem. Phys.* 13 (2011) 136–143.
- [25] W. Wang, C. Lu, Y. Ni, M. Su, W. Huang, Z. Xu, *Appl. Surf. Sci.* 258 (2012) 8696–8703.
- [26] X. Cheng, X. Yu, Z. Xing, *Mater. Res. Bull.* 47 (2012) 3804–3809.
- [27] F.T. Li, X.J. Wang, Y. Zhao, J.X. Liu, Y.J. Hao, R.H. Liu, D.S. Zhao, *Appl. Catal. B: Environ.* 144 (2014) 442–453.
- [28] G. Grigoropoulou, K.C. Christoforidis, M. Louloudi, Y. Deligiannakis, *Langmuir* 23 (2007) 10407–10418.
- [29] J.M. Warman, M.P. de Haas, P. Picbat, N. Serpone, *J. Phys. Chem.* 95 (1991) 8858–8861.
- [30] N. Wang, Y. Xu, L. Zhu, X. Shen, H.J. Tang, *Photochem. Photobiol. A: Chem.* 201 (2009) 121–127.
- [31] H.M. Rietveld, *Acta Cryst.* 22 (1967) 151–152.
- [32] N. Di Li, S. Ohashi, T. Hishita, H. Kolodiazhyi, J. Haneda, *Solid State Chem.* 178 (2005) 3293–3302.
- [33] T. Berger, M. Sterrer, O. Diwald, E. Knozinger, D. Panayotov, T.L. Thompson, J.T. Yates Jr., *J. Phys. Chem. B* 109 (2005) 6061–6068.
- [34] J.M. Coronado, A.J. Maira, J.C. Conesa, K.L. Yeung, V. Augugliaro, J. Soria, *Langmuir* 17 (2001) 5368–5374.
- [35] S. Livraghi, M.C. Paganini, E. Giamello, A. Selloni, C. Di Valentin, G. Pacchioni, *J. Am. Chem. Soc.* 128 (2006) 15666–15671.
- [36] M. Fittipaldi, V.T. Gombac, P. Montini, M. Fornasiero, Graziani, *Inorg. Chim. Acta* 361 (2008) 3980–3987.
- [37] S. Won Ahn, K.H. Kang, D.I. Hong, *J. Korean Magn. Res. Soc.* 4 (2000) 50–63.
- [38] L.B. Xiong, J.-L. Li, B. Yang, Y. Yu, *J. Nanomat.* Volume 2012, Article ID 831524, 13 pages doi:10.1155/2012/831524.
- [39] J. Zhang, Z. Jin, C. Feng, L. Yu, J. Zhang, Z. Zhang, *J. Solid State Chem.* 184 (2011) 3066–3073.
- [40] Z. Zhang, J. Long, X. Xie, H. Zhuang, Y. Zhou, H. Lin, R. Yuan, W. Dai, Z. Ding, X. Wang, X. Fu, *Appl. Catal. A: Gen.* 425–426 (2012) 117–124.
- [41] G. Barolo, S. Livraghi, M. Chiesa, M.C. Paganini, E. Giamello, *J. Phys. Chem. C* 116 (2012) 20887–20894.
- [42] A. Ajmera, S.B. Sawant, V.G. Pangarkar, A.A.C.M. Beenackers, *Chem. Eng. Technol.* 25 (2002) 173–180.
- [43] A. Assabane, Y. Ait Ichou, H. Tahir, C. Guillard, J.M. Herrmann, *Appl. Catal. B: Environ.* 24 (2000) 71–87.
- [44] J.G. Yu, W.G. Wang, B. Cheng, B.L. Su, *J. Phys. Chem. C* 113 (2009) 6743–6750.
- [45] G. Liu, Y. Zhao, C. Sun, F. Li, G.Q. Lu, H.-M. Cheng, *Angew. Chem. Int. Ed.* 47 (2008) 4516–4520.
- [46] Y.M. Wu, M.Y. Xing, J.L. Zhang, *J. Hazard. Mat.* 192 (2011) 368.
- [47] N. Feng, A. Zheng, Q. Wang, P. Ren, X. Gao, S.-B. Liu, Z. Shen, T. Chen, F. Deng, *J. Phys. Chem. C* 115 (2011) 2709–2719.